2024 IEEE/RSJ International Conference on Intelligent Robots and Systems (IROS)
October 14-18, 2024. Abu Dhabi, UAE

Design of a Fully Actuated Drone with Non-Isotropic Wrench Shape

Seongsu Park and Min Jun Kim

Abstract— **This paper proposes a novel design framework for a fully actuated drone with non-isotropic wrench shape. Conventional fully actuated drones face challenges related to high energy consumption during aerial contact manipulation, particularly when force exertion along a specific direction is required. This challenge arises from the balanced tilting of propellers, which leads to an isotropic wrench shape. To address this limitation, we explicitly define the required wrench set (RW) for aerial contact manipulation and integrate it into an optimization problem. To ensure the generation of the RW, we employ the hyperplane shifting method, commonly used for verifying wrench feasibility in cable-driven robots. The optimization aims to minimize hovering energy consumption while ensuring wrench feasibility. Consequently, the proposed design demonstrates a significant improvement over the typical fully actuated drone, with hovering and contact force efficiency more than doubled and nearly 1.4 times higher, respectively. The effectiveness of our design is also validated through simulation.**

I. INTRODUCTION

In recent decades, there has been extensive research on drones for various passive missions such as monitoring, mapping, and surveillance. Moreover, efforts have been made to utilize drones for active missions that involve physical interactions such as aerial contact inspection shown in Fig. 1. However, typical drones may suffer from significant control challenges during contact manipulation due to the under-actuation resulting from the collinear arrangement of their propellers [1]–[3]. To overcome this, a number of studies have been conducted to design fully actuated drones, which generate multi-directional thrust by transforming the collinear propellers into a non-collinear arrangement [4], [5].

To design a fully actuated drone, numerous studies have utilized an optimization-based approach, considering various objectives and constraints [6]–[13]. Several works have employed additional actuator to accomplish both under-actuation and full actuation [14]–[16]. While various variants have been proposed [17]–[19], a standard form of fully actuated drone involves propellers with non-collinear directions.

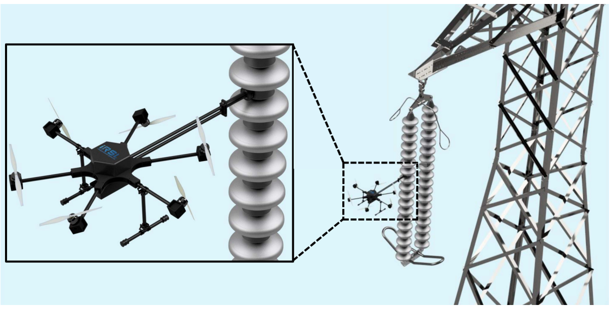
Fig. 1. Example of aerial contact manipulation that requires to apply constant force to the environment.

However, these drones [6]–[10], [14]–[16] can only generate isotropic wrench shape[1] due to the balanced propeller shapes. Such designs inherently suffer from force cancellation because tilted propellers are facing each other, resulting in lower hovering efficiency compared to the conventional under-actuated systems. These limitations become more severe when aerial contact manipulation is of interest. For example, consider a task requiring significant contact force for inspecting an object, as shown in Fig. 1. To generate the desired contact force, all the propellers must be extensively tilted. These extensive tiltings result in high energy consumption for hovering and contact manipulation. As a result, standard fully actuated drones may encounter challenges when dealing with tasks demanding substantial contact force.

To mitigate such limitations, in this paper, we propose a novel design approach for a fully actuated drone that can generate a non-isotropic wrench shape. The main novelty lies in generating a prescribed wrench set required for performing contact manipulation with higher hovering force efficiency compared to existing fully actuated systems. To ensure the generation of the required wrench set, we employ the hyperplane shifting method, which is commonly used in cable-driven robots for verifying wrench feasibility. To achieve higher hovering force efficiency than standard fully actuated drones, the energy consumed for hovering is considered as a cost function in the optimization problem.

To the best of our knowledge, this paper presents the first systematic effort to create a non-isotropic wrench shape for fully actuated drones. Compared to existing works [11]–[13], we explicitly define the required wrench set based on the given task. Subsequently, the tilting of propellers is optimized while ensuring the generation of the required wrench set

---

This work was supported in part by the National Research Foundation of Korea (NRF) grant funded by the Korea government (MSIT) under Grant 2021R1C1C1005232, and in part by the ITECH R&D program of MOTIE/KEIT (Project No. 20014398, Development of a kinematically versatile, easy-to-use, safety-supported, AI-integrable, and high speed (>=5kHz) robot controller).

The authors are with Intelligent Robotic Systems Laboratory, Korea Advanced Institute of Science and Technology (KAIST), Daejeon, Republic of Korea. E-mail: `seongsu.park@kaist.ac.kr`, `minjun.kim@kaist.ac.kr`

[1] To be precise, the generated force and torque envelopes exhibit a laterally isotropic shape with respect to (w.r.t.) the body frame in X-Y plane. When considering gravitational force, the force and torque envelopes are anisotropic in three dimensions, respectively.

979-8-3503-7769-9/24/$31.00 ©2024 IEEE

and minimizing the hovering thrust forces. This approach results in a non-isotropic wrench shape and reduces energy consumption during hovering. In validation, our proposed drone demonstrates that the hovering force efficiency is more than doubled, and the contact force efficiency is nearly 1.4 times higher than that of the typical drone when both are designed to exert a force of $45\mathrm{N}$ along the $+x$ direction.

This paper is organized as follows. Section II presents the system modeling of the generic drone system and wrench feasibility with the hyperplane shifting method. In Section III, we define the required wrench set for aerial contact manipulation and present the optimization problem to satisfy wrench feasibility. In Section IV, we present the optimized wrench shape and its corresponding propeller configurations, and compare the hovering and contact force efficiency, along with the isotropic wrench shape. At last, we validate its effectiveness using the hybrid wrench and pose control in simulation.

II. BACKGROUND

A. System modeling

Consider a drone system shown in Fig. 2. We define an inertial world frame as $\mathcal{F}_W : \{O_W, X_W, Y_W, Z_W\}$ where O_W denotes its origin. The body frame is defined as $\mathcal{F}_B : \{O_B, X_B, Y_B, Z_B\}$ which is rigidly attached to the vehicle's center of mass (CoM). The position of O_B and orientation of $\mathcal{F}_B$ w.r.t. $\mathcal{F}_W$ are represented by the vector $\boldsymbol{p}_B \in \mathbb{R}^3$ and the rotation matrix $\boldsymbol{R}_B \in SO(3)$, respectively. The body angular velocity of $\mathcal{F}_B$ is denoted as $\boldsymbol{\omega}_B \in \mathbb{R}^3$.

The system is modeled as a rigid body with mass $m \in \mathbb{R}_+$ and moment of inertia $\boldsymbol{J} \in \mathbb{R}^{3\times 3}$ w.r.t. $\mathcal{F}_B$. By using the Newton-Euler equations with $\dot{\boldsymbol{p}}_B = \boldsymbol{v}_B$ and $\dot{\boldsymbol{R}}_B = \boldsymbol{R}_B \hat{\boldsymbol{\omega}}_B$, where the hat operator $\widehat{(\cdot)} : \mathbb{R}^3 \mapsto \mathfrak{so}(3)$ such that $\hat{\boldsymbol{a}}\boldsymbol{b} = \boldsymbol{a} \times \boldsymbol{b}$ for all $\boldsymbol{a}, \boldsymbol{b} \in \mathbb{R}^3$, the equation of motion of the drone system is written as:

$$\begin{bmatrix} m\dot{\boldsymbol{v}}_B \\ \boldsymbol{J}\dot{\boldsymbol{\omega}}_B \end{bmatrix} = -\begin{bmatrix} mg\boldsymbol{e}_3 \\ \boldsymbol{\omega}_B \times \boldsymbol{J}\boldsymbol{\omega}_B \end{bmatrix} + \begin{bmatrix} \boldsymbol{R}_B \boldsymbol{f} \\ \boldsymbol{\tau} \end{bmatrix}, \tag{1}$$

where $\boldsymbol{e}_3 = [0,\ 0,\ 1]^T$, g is gravity constant, $\boldsymbol{f} \in \mathbb{R}^3$ and $\boldsymbol{\tau} \in \mathbb{R}^3$ are the control force and torque expressed in $\mathcal{F}_B$.

In a drone system with n rotors, the control input consists of the thrust force of each rotor, denoted as $\boldsymbol{u} = [u_1,\ \dots, u_n]^T \in \mathbb{R}^n$. The rotor input $\boldsymbol{u}$ can be mapped to the body wrench $\mathbf{w} = [\boldsymbol{f}^T\ \boldsymbol{\tau}^T]^T \in \mathbb{R}^6$ using the *full allocation matrix* $\boldsymbol{A} \in \mathbb{R}^{6\times n}$,

$$\mathbf{w} = \boldsymbol{A}\boldsymbol{u} = \begin{bmatrix} \boldsymbol{A}_{\boldsymbol{f}} \\ \boldsymbol{A}_{\boldsymbol{\tau}} \end{bmatrix} \boldsymbol{u}. \tag{2}$$

The matrices $\boldsymbol{A}_{\boldsymbol{f}} \in \mathbb{R}^{3\times n}$ and $\boldsymbol{A}_{\boldsymbol{\tau}} \in \mathbb{R}^{3\times n}$ are referred to as *force allocation matrix* and *moment allocation matrix*, respectively. Each allocation matrix has the following structure:

$$\boldsymbol{A}_{\boldsymbol{f}} = \ [\boldsymbol{v}_1,\ \dots, \boldsymbol{v}_n], \tag{3}$$

$$\boldsymbol{A}_{\boldsymbol{\tau}} = \ [\boldsymbol{r}_1 \times \boldsymbol{v}_1 + \sigma_1 k_1 \boldsymbol{v}_1,\ \dots, \boldsymbol{r}_n \times \boldsymbol{v}_n + \sigma_n k_n \boldsymbol{v}_n], \tag{4}$$

where $\boldsymbol{v}_i \in \mathbb{R}^3$ represents the thrust unit vector generated by the i^{th} propeller, $\boldsymbol{r}_i$ denotes the position of the i^{th} propeller center in body frame. In addition, σ_i indicates the spinning axis of the propeller, and $k_i = c_d/c_f$ is the constant ratio between the i^{th} propeller lift coefficient c_f and drag coefficient c_d. Note that $\sigma_i = -1$ if the i^{th} propeller's angular velocity vector has the same direction $\boldsymbol{v}_i$, and if not, $\sigma_i = 1$.

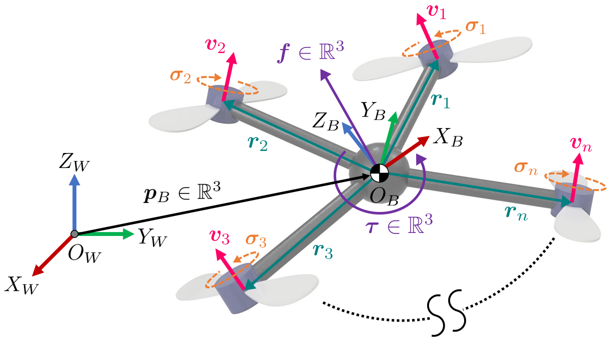

Fig. 2. Schematic representation of generic drone with n propellers.

B. Wrench feasibility

In cable-driven robot literature, a set of wrenches that the mobile robot must be able to generate in a particular pose is denoted as the required wrench set (RW). On the other hand, the available wrench set (AW) is generally defined as the set of all feasible wrenches:

$$AW = \{\mathbf{w} = \boldsymbol{\Lambda}\boldsymbol{t} \,|\, \boldsymbol{t}_{\min} \preceq \boldsymbol{t} \preceq \boldsymbol{t}_{\max}\}, \tag{5}$$

where $\boldsymbol{t}_{\min}$ and $\boldsymbol{t}_{\max}$ are vectors representing the minimum and maximum cable tensions, and $\boldsymbol{\Lambda} \in \mathbb{R}^{6\times n}$ maps cable tension vectors to the wrench $\mathbf{w}$ of the mobile robot [20]. In addition, $\preceq$ denotes a component-wise inequality between two vectors of the same dimension.

A pose of a mobile robot is considered *wrench-feasible* when the AW completely contains the RW [20]–[22]:

$$RW \subseteq AW. \tag{6}$$

Similar to the cable-driven robot, the drone system generates a body wrench through the full allocation matrix when rotor input is provided, as in (2). By utilizing this analogy, the set of all feasible wrenches for a drone can be expressed as:

$$AW = \{\mathbf{w} = \boldsymbol{A}\boldsymbol{u} \,|\, \boldsymbol{u}_{\min} \preceq \boldsymbol{u} \preceq \boldsymbol{u}_{\max}\}, \tag{7}$$

where $\boldsymbol{u}_{\min}$ and $\boldsymbol{u}_{\max}$ are minimum and maximum thrust force vectors, respectively. In fact, since we are focusing on the drone system with unidirectional thrusters, let us assume $\boldsymbol{u}_{\min} = \mathbf{0}$. If the drone needs to generate a wrench $\mathbf{w} \in RW$ at a particular pose, and if this wrench is contained in AW, then that particular pose of the drone system is considered wrench-feasible.

C. Hyperplane shifting method

It is challenging to determine all the feasible rotor input $\boldsymbol{u} \in [\boldsymbol{u}_{\min}, \boldsymbol{u}_{\max}]$ capable of generating every $\mathbf{w} \in RW$ by using (7). To address this, the *hyperplane shifting method* can be applied. The hyperplane shifting method involves modifying the equation (7) to a set of linear inequalities as:

$$AW = \{\mathbf{w} \,|\, \boldsymbol{C}\mathbf{w} \preceq \boldsymbol{d}\}. \tag{8}$$

The matrix $\boldsymbol{C} \in \mathbb{R}^{\alpha \times 6}$ and vector $\boldsymbol{d} \in \mathbb{R}^{\alpha}$ with $\alpha = 2 \times {}_n\mathrm{C}_5$, represent the matrix composed of normal vectors defining each hyperplane of AW, and the vector representing the maximum distances from the origin to the associated hyperplane along its respective normal vector, respectively [13], [20], [21]. Utilizing this set of inequalities allows straightforward verification of wrench feasibility. By substituting a wrench vector $\mathbf{w} \in RW$ into (8) and verifying the resulting inequalities, the wrench feasibility can be verified.

1) Three-dimensional case: Although this paper focuses on the six-dimensional case, let us start with the three-dimensional case for a step-by-step presentation. In Fig. 3, for instance, consider a gray-colored force envelope that a point mass drone can generate with thrust unit vectors along $\boldsymbol{v}_1$, $\boldsymbol{v}_2$, and $\boldsymbol{v}_3$ directions. Each row of $\boldsymbol{C} \in \mathbb{R}^{6\times3}$, where $\boldsymbol{C} = [\boldsymbol{c}_1, \dots, \boldsymbol{c}_6]^T$, corresponds to the transpose of a unit normal vector defining a plane of the force envelope. To verify the wrench feasibility w.r.t. each plane of the envelope, the process involves projecting a force vector $\mathbf{f}_a$ onto its respective normal vector $\boldsymbol{c}_j$. If the projected value is smaller than d_1 of $\boldsymbol{d} \in \mathbb{R}^6$, where $d_1 = u_{\max}\boldsymbol{c}_1^T\boldsymbol{v}_1$, the wrench feasibility w.r.t. that plane of the force envelope is satisfied. This procedure is repeated for every plane of the force envelope to verify the wrench feasibility.

2) Six-dimensional case: To obtain the matrix $\boldsymbol{C}$ and vector $\boldsymbol{d}$ in six-dimensional wrench space, let us first consider the full allocation matrix $\boldsymbol{A} \in \mathbb{R}^{6\times n}$ with $n \geq 6$, assuming it is a full-rank matrix. To determine $\boldsymbol{C}$, we should select each combination of five linearly independent columns from $\boldsymbol{A}$ [20], [21]:

$$\boldsymbol{A}_I = [\boldsymbol{a}_{i_1}\ \boldsymbol{a}_{i_2}\ \boldsymbol{a}_{i_3}\ \boldsymbol{a}_{i_4}\ \boldsymbol{a}_{i_5}]^T, \tag{9}$$

where $\boldsymbol{A}_I \in \mathbb{R}^{5\times6}$ and I denotes the index set $\{i_1, \dots, i_5\} \subset \{1, \dots, n\}$. By utilizing the nullspace of $\boldsymbol{A}_I$, we can obtain the two vectors, denoted as $\boldsymbol{c}_p \in \mathbb{R}^6$ and $\boldsymbol{c}_q \in \mathbb{R}^6$, of $\boldsymbol{C}$:

$$span(\boldsymbol{c}_p) = span(-\boldsymbol{c}_q) = null(\boldsymbol{A}_I). \tag{10}$$

Note that these two vectors are opposite, as a single plane can have two normal vectors pointing in opposite directions. The matrix $\boldsymbol{C}$, in turn, has the form of $\boldsymbol{C} \in \mathbb{R}^{\alpha\times6}$, where $\alpha = 2 \times {}_n\mathrm{C}_5$.

To determine d_j of $\boldsymbol{d}$ corresponding to $\boldsymbol{c}_j^T$ of $\boldsymbol{C}$, the following optimization problem can be considered [23]:

$$d_j = \max_{u_1, \dots, u_n} \sum_{k=1}^{n} u_k \boldsymbol{c}_j^T \boldsymbol{a}_k, \tag{11}$$

where $\boldsymbol{a}_k$ is the k^{th} column of $\boldsymbol{A}$ and $u_k \in [u_{\min}, u_{\max}]$. Upon expanding (11), d_j can be expressed as:

$$d_j = \sum_{i \in I_j^+} u_{\max}\boldsymbol{c}_j^T\boldsymbol{a}_i + \sum_{i \in I_j} u_{\min}\boldsymbol{c}_j^T\boldsymbol{a}_i, \tag{12}$$

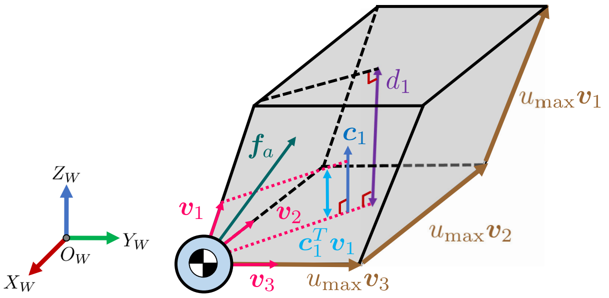

Fig. 3. Force envelope generated by three $\boldsymbol{v}_i$ vectors from a point mass drone and its description for a single plane using the hyperplane shifting method.

where I_j^+ and I_j^- are subsets of $\{1, \dots, n\}$ defined as $I_j^+ = \{i \,|\, \boldsymbol{c}_j^T\boldsymbol{a}_i > 0\}$ and $I_j^- = \{i \,|\, \boldsymbol{c}_j^T\boldsymbol{a}_i < 0\}$. Considering $u_{\min} = 0$, d_j can be written as:

$$d_j = \sum_{i=1}^{n} \max(0, u_{\max}\boldsymbol{c}_j^T\boldsymbol{a}_i). \tag{13}$$

III. NON-ISOTROPIC WRENCH SHAPE DESIGN

In this paper, we consider aerial contact manipulation, which requires a static contact force while maintaining a fixed pose of the system. To ensure the generation of static contact force without torque, when explicitly defining RW, we define it as the required force set with zero torque in Section III-A. In Section III-B, we present the optimization problem for AW to fully encompass the predefined RW using (8), and discuss its implementation in Section III-C.

A. Required wrench set

1) Static hovering: Let us represent the wrench vector as $\mathbf{w} = [f_x, f_y, f_z, \tau_x, \tau_y, \tau_z]^T$. To define the RW for static hovering, the following conditions must be satisfied [24]:

$$\dot{\boldsymbol{p}}_B = \boldsymbol{0},\ \boldsymbol{A_f u} = \boldsymbol{R}_B^T mg\boldsymbol{e}_3,\ \boldsymbol{w}_B = \boldsymbol{0},\ \boldsymbol{A_\tau u} = \boldsymbol{0}. \tag{14}$$

During static hovering, a drone must be able to generate mg in the z-direction of the inertial frame. However, considering that the AW is defined w.r.t. the body frame of the drone system, the RW for static hovering should be represented by the gravity in the body frame. In other words, the RW w.r.t. the rotation $\boldsymbol{R}_B$ is expressed as $\boldsymbol{R}_B^T mg\boldsymbol{e}_3$ with zero torque. Hence, in this paper, to simplify the definition of static hovering without loss of generality, $\boldsymbol{R}_B$ is set to the $\boldsymbol{I}_3$. Then, the RW for static hovering RW_{hover} becomes:

$$\begin{aligned} RW_{\text{hover}} = \{\mathbf{w} \,|\, & f_z = mg, \\ & f_x = f_y = \tau_x = \tau_y = \tau_z = 0\}. \end{aligned} \tag{15}$$

2) Horizontal forces while hovering: Unlike under-actuated drones, fully actuated drones can generate horizontal forces while maintaining their pose. This capability for force exertion can be utilized for, e.g., physical interaction with the environment and disturbance rejection. We define the RW for horizontal force capability as:

$$\begin{aligned} RW_{\text{h}} = \{\mathbf{w} \,|\, & \sqrt{f_x^2 + f_y^2 + f_z^2} \leq F_{\text{h}}, \\ & \tau_x = \tau_y = \tau_z = 0\}, \end{aligned} \tag{16}$$

where F_h represents the magnitude of the horizontal force exerted on the system.

Verifying whether all wrenches $\mathbf{w} \in RW_\mathrm{h}$ satisfy equation (8) is impractical. Hence, we need to reorganize (16) to ensure wrench feasibility using (8). To reorganize (16), we utilize the convexity of RW_h and AW. Given that both sets are convex, when the boundary values of RW_h are entirely contained within AW, the inner values of RW_h inherently satisfy the wrench feasibility. As a result, by using the equation (8), we can derive the f_x, f_y, and f_z of RW_h as:

$$f_x = \frac{F_\mathrm{h} c_{j_1}}{\sqrt{c_{j_1}^2 + c_{j_2}^2 + c_{j_3}^2}},\ f_y = \frac{F_\mathrm{h} c_{j_2}}{\sqrt{c_{j_1}^2 + c_{j_2}^2 + c_{j_3}^2}},$$

$$f_z = \frac{F_\mathrm{h} c_{j_3}}{\sqrt{c_{j_1}^2 + c_{j_2}^2 + c_{j_3}^2}}. \tag{17}$$

For derivation, please refer to Appendix A.

To achieve static hovering while considering the generation of horizontal forces, both static hovering and horizontal force capability should be considered simultaneously. Hence, we define the RW for static hovering and horizontal force capability, denoted as $RW_\mathrm{h.hov}$:

$$RW_\mathrm{h.hov} = RW_\mathrm{hover} \oplus RW_\mathrm{h}, \tag{18}$$

where $\oplus$ denotes the Minkowski sum. Utilizing equations (15) and (17), we can represent the wrench $\mathbf{w} = [f_x,\ f_y,\ f_z,\ \tau_x,\ \tau_y,\ \tau_z]^T \in RW_\mathrm{h.hov}$ as:

$$f_x = \frac{F_\mathrm{h} c_{j_1}}{\sqrt{c_{j_1}^2 + c_{j_2}^2 + c_{j_3}^2}},\ f_y = \frac{F_\mathrm{h} c_{j_2}}{\sqrt{c_{j_1}^2 + c_{j_2}^2 + c_{j_3}^2}},$$

$$f_z = \frac{F_\mathrm{h} c_{j_3}}{\sqrt{c_{j_1}^2 + c_{j_2}^2 + c_{j_3}^2}} + mg,\ \tau_x = \tau_y = \tau_z = 0. \tag{19}$$

3) Contact force: Recall that the primary component underlying the creation of a non-isotropic wrench shape is to define the contact force. When the contact force is neglected in RW, it forms a force sphere at mg with zero torque, denoted as $RW_\mathrm{h.hov}$. However, incorporating the contact force into the definition of RW results in a non-isotropic wrench shape oriented towards the direction of the contact force. The definition of RW_contact can vary depending on the requirements. In our case, we focus on a scenario where aerial contact manipulation requires static contact force along the $+x$-axis w.r.t. the inertial frame. Therefore, RW_contact is defined as:

$$\begin{aligned} RW_\mathrm{contact} = \{\mathbf{w} \,|\, & f_x = F_\mathrm{c},\ f_z = mg, \\ & f_y = \tau_x = \tau_y = \tau_z = 0\}, \end{aligned} \tag{20}$$

where F_c represents the magnitude of the contact force that the drone should generate.

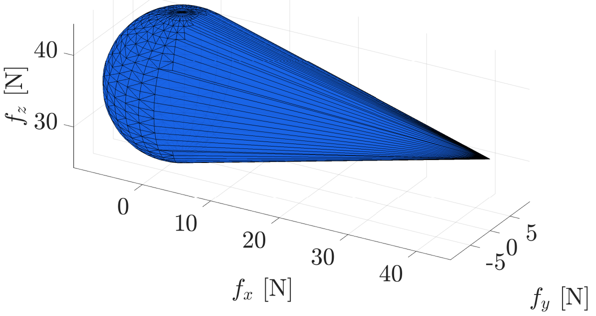

Fig. 4. The set of total required forces with zero torque: RW_total.

4) Total required wrench set: To visualize the total required wrench set RW_total, which includes both $RW_\mathrm{h.hov}$ and RW_contact, we use the convex hull method in Fig. 4. Since RW_total exhibits a convex shape, it is unnecessary to verify all $\mathbf{w} \in RW_\mathrm{total}$ for wrench feasibility using (8). By employing the properties of convex polytopes, if the set of linear inequalities resulting from substituting (19) and (20) into (8) holds true, wrench feasibility is satisfied. Therefore, it is sufficient to consider only the wrenches $\mathbf{w} \in RW_\mathrm{h.hov}$ and $\mathbf{w} \in RW_\mathrm{contact}$ for wrench feasibility.

B. Optimization formulation

The goal of our design optimization is to determine thrust unit vectors that allow the containment of RW within AW while minimizing the hovering energy consumption. To this end, we formulate a constrained nonlinear optimization problem as:

$$\min_{\boldsymbol{v}_1,\ \dots\ ,\boldsymbol{v}_n,\boldsymbol{u}_h} \quad \sum_{i=1}^{n} u_{h_i}^{3/2} \tag{21a}$$

$$\text{subject to} \quad \boldsymbol{C}\mathbf{w} \preceq \boldsymbol{d},\ \mathbf{w} \in RW_\mathrm{total} \tag{21b}$$

$$\boldsymbol{v}_i^T \boldsymbol{v}_i = 1 \tag{21c}$$

$$\boldsymbol{A}\boldsymbol{u}_h = \ [0,\ 0,\ mg,\ 0,\ 0,\ 0]^T \tag{21d}$$

$$\boldsymbol{u}_\mathrm{min} \preceq \boldsymbol{u}_h \preceq \boldsymbol{u}_\mathrm{max}. \tag{21e}$$

The decision variables $\boldsymbol{v}_i$ and $\boldsymbol{u}_h$, where $\forall i = 1, 2, \dots, n$, represent the thrust unit vectors and hovering thrust forces, respectively. The goal of (21a) is to determine optimal thrust directions while minimizing the hovering power. The cost function can be physically interpreted as the power consumed by an actuator for static hovering, given that the power P_i is related to its thrust force, expressed as $P_i \propto u_i^{3/2}$ [25].

Regarding the constraints, (21b) guarantees wrench feasibility $RW_\mathrm{total} \subseteq AW$, and (21c) ensures that the norm of the i^{th} thrust unit vector remains at one, while constraints (21d) and (21e) represent the hovering condition and the thrust limit constraints, respectively. For a fully actuated drone with six rotors, the full allocation matrix is a six-by-six full rank matrix, resulting in a unique solution for $\boldsymbol{u}_h$. However, when the number of rotors exceeds six, the full allocation matrix exhibits redundancy, thereby permitting multiple solutions for $\boldsymbol{u}_h$. Hence, the equations (21d) and (21e) are added

TABLE I

PARAMETERS FOR OPTIMIZATION AND OPTIMIZED VALUES

Description	Symbol	Value	Unit
Parameters	m	3.5	kg
	u_{min}	0.0	N
	u_{max}	25.3095	N
	c_f	2.2718×10^{-5}	Ns^2
	c_d	3.5765×10^{-7}	Nms^2
	n	6	–
	l	800	mm
	F_{h}	10.0	N
	F_{c}	45.0	N
Optimized values	$\boldsymbol{v}_i$	$\boldsymbol{v}_1 = [-0.4412,\ 0.2485,\ 0.8623]^T$ $\boldsymbol{v}_2 = [0.9261,\ 0.1368,\ 0.3516]^T$ $\boldsymbol{v}_3 = [-0.1042, -0.3842, 0.9174]^T$ $\boldsymbol{v}_4 = [-0.4412,\ 0.2485,\ 0.8623]^T$ $\boldsymbol{v}_5 = [0.9261,\ 0.1368,\ 0.3516]^T$ $\boldsymbol{v}_6 = [-0.1042, -0.3842, 0.9174]^T$	–
	$\boldsymbol{u}_h$	$u_{h_1} = 9.3109 \quad u_{h_2} = 5.3271$ $u_{h_3} = 7.9202 \quad u_{h_4} = 9.3109$ $u_{h_5} = 5.3271 \quad u_{h_6} = 7.9202$	N

as constraints to fully utilize the redundancy of the full allocation matrix for hovering.

C. Implementation

To implement the optimization, let us first define the position vectors of each propeller, denoted as $\mathbf{r}_i$ for the i^{th} propeller:

$$\mathbf{r}_i = \mathbf{R}_z(\psi_i) \begin{bmatrix} l/2 \\ 0 \\ 0 \end{bmatrix}, \quad \forall i = 1, 2, \ldots, n, \tag{22}$$

where $\psi_i = \pi(2i-1)/n$ and $l/2$ denotes the distance from the center of mass to the rotating axis of the propeller. $\mathbf{R}_z(\psi) \in SO(3)$ represents the canonical rotation matrix about the z-axis by an angle ψ. Additionally, we consider the spinning axis of each propeller as $\sigma_i = (-1)^i$ for simplicity. Further parameters essential for solving the optimization problem are listed in Table I.

To employ a gradient-based solver for the nonlinear constrained optimization problem (21a)-(21e), we approximate $\max(0, u_{\text{max}} \boldsymbol{c}_j^T \boldsymbol{a}_i)$ in (13) as:

$$\max(0, u_{\text{max}} \boldsymbol{c}_j^T \boldsymbol{a}_i) \simeq \frac{u_{\text{max}} \boldsymbol{c}_j^T \boldsymbol{a}_i + \sqrt{(u_{\text{max}} \boldsymbol{c}_j^T \boldsymbol{a}_i)^2 + \epsilon}}{2}, \tag{23}$$

where $\epsilon \geq 0$. As ϵ becomes smaller, higher approximation accuracy is achieved. In the implementation, we utilize the interior point (IP) algorithm in MATLAB, incorporating the approximation function. Since this approach typically converges to a local minimum, the process is repeated to obtain a better solution among several local minima acquired from each use of the IP method with randomly chosen initial guesses.

IV. OPTIMIZATION RESULT AND VALIDATION

The optimized thrust unit vectors and hovering thrust force were obtained, as presented in Table I. To compare the proposed non-isotropic case with a typical isotropic one, we conducted the same optimization for the conventional drone, utilizing balanced propeller shapes as a constraint. We compare the performance of isotropic and non-isotropic cases in terms of hovering and contact force efficiency, as well as their wrench shapes and propeller configurations, in Section IV-A. In Section IV-B, simulation is conducted to verify the wrench feasibility of RW_{total}.

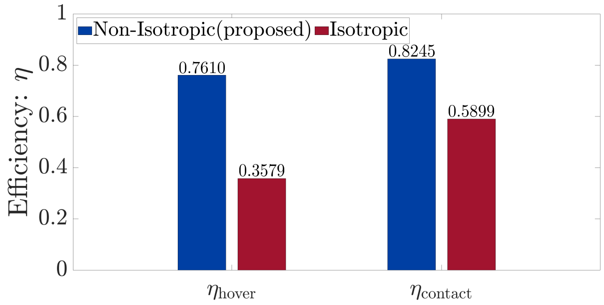

Fig. 5. Force efficiency: Hovering at $[0,\ 0,\ mg]^T$ and contact force at $[45,\ 0,\ mg]^T$ with zero torque.

A. Hovering and contact force efficiency

The force efficiency of the drone is defined as [14]:

$$\eta_f = \frac{\|\boldsymbol{f}_d\|}{\sum_{i=1}^{n} u_i} \in [0, 1], \tag{24}$$

where η_f is the ratio of the norm of the desired force $\boldsymbol{f}_d$ to the sum of all thrust forces required to generate that force. Therefore, the ratio η_f can be interpreted as the degree of force cancellation between the propellers.

Using (24), we computed the hovering efficiency at $\boldsymbol{f}_d = [0,\ 0,\ mg]^T$ and the contact force efficiency at $\boldsymbol{f}_d = [45,\ 0,\ mg]^T$ with zero torque, as shown in Fig. 5. The proposed non-isotropic case shows better performance in both hovering and contact force efficiency compared to the typical isotropic case, more than doubling the hovering force efficiency. As a result, the proposed AW_f demonstrates a broader capability for exerting force in the $+z$ direction compared to the isotropic AW, as shown in Fig. 6(a) and 6(b). In fact, our approach enables the exertion of forces of approximately 107.8N, which is nearly double the $+z$ force capability of a typical isotropic case, where the capacity is around 54.3N in the $+z$ direction.

Regarding the propeller configurations of drones corresponding to each AW, as shown in Fig. 6(c) and 6(d), the conventional drone shows all its propellers extensively tilted in a balanced manner. In contrast, the proposed drone demonstrates that only the second and fifth propellers are extensively tilted towards the contact direction to generate the desired force, while the remaining propellers are tilted less to improve hovering force efficiency.

When comparing the proposed AW_f with the isotropic AW_f from a top view in Fig. 7, our non-isotropic case tightly contains RW_{total}, resulting in a relatively narrow force shape in the f_y direction, while the isotropic case shows a significantly wider horizontal force shape. The proposed

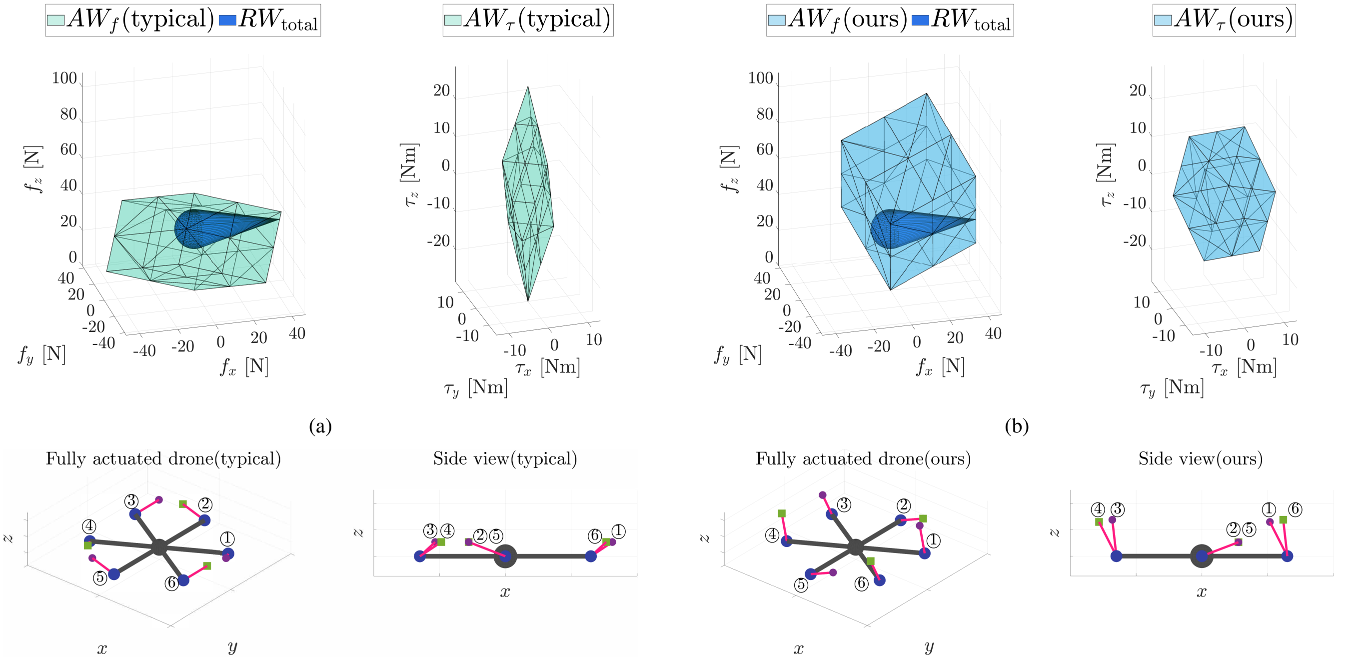

(a) (b)

(c) (d)

Fig. 6. (a) Typical isotropic wrench shape with RW_{total} (b) Proposed non-isotropic wrench shape with RW_{total}. (c) Fully actuated drone design with isotropic wrench shape. (d) Fully actuated drone design with non-isotropic wrench shape. The blue spheres represent the placement of the rotors. The pink lines represent the thrust direction of each rotor. The purple sphere denotes the counterclockwise (CCW) propeller, and the green square denotes the clockwise (CW) propeller.

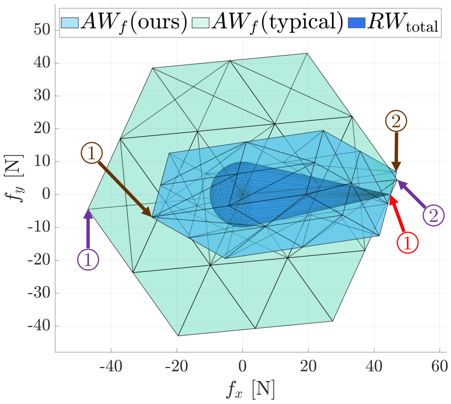

Fig. 7. Top view: Non-isotropic AW_f(ours), isotropic AW_f(typical), and RW_{total}. The f_x indicated by the red arrow is 45N. The f_x indicated by the first and second brown and purple arrows are 27.60N, 46.87N, 47.05N, and 47.05N, respectively.

AW_f exhibits a wide range of $+f_x$ direction, similar to the isotropic AW_f, while the difference is pronounced in the $-f_x$ direction. In fact, the proposed AW_f can generate f_x of -27.60N and 46.87N at the respective brown arrows ① and ②, whereas the isotropic AW_f can exert f_x of -47.05N and 47.05N at each purple arrow ① and ②. This difference stems from the imposition of balanced propeller shapes on the isotropic AW_f during optimization, which leads to lower hovering and contact force efficiency.

B. Simulation validation

In this section, we validate that the designed fully actuated drone can indeed generate the required contact wrench while satisfying thrust saturation. We added a rigid bar to the center of mass of the proposed system and implemented hybrid wrench and pose control for an aerial contact scenario. By employing PI and PD control for wrench and pose control with selection matrices $\mathbf{S}_w \in \mathbb{R}^{6\times6}$ and $\mathbf{S}_p \in \mathbb{R}^{6\times6}$, the control law is given by:

$$\mathbf{w} = \boldsymbol{S}_w \begin{bmatrix} \boldsymbol{f}_w \\ \boldsymbol{\tau}_w \end{bmatrix} + \boldsymbol{S}_p \begin{bmatrix} \boldsymbol{f}_p \\ \boldsymbol{\tau}_p \end{bmatrix}, \tag{25}$$

where

$$\begin{aligned} \boldsymbol{f}_w &= \boldsymbol{f}_d - \boldsymbol{K}_{P,f}\boldsymbol{e}_f - \boldsymbol{K}_{I,f}\int \boldsymbol{e}_f d\tau, \\ \boldsymbol{\tau}_w &= \boldsymbol{\tau}_d - \boldsymbol{K}_{P,m}\boldsymbol{e}_m - \boldsymbol{K}_{I,m}\int \boldsymbol{e}_m d\tau \end{aligned} \tag{26}$$

for wrench control, and

$$\begin{aligned} \boldsymbol{f}_p &= -mg\boldsymbol{e}_3 - \boldsymbol{K}_{P,t}\boldsymbol{e}_t - \boldsymbol{K}_{D,t}\dot{\boldsymbol{e}}_t, \\ \boldsymbol{\tau}_p &= \boldsymbol{w}_B \times \boldsymbol{J}\boldsymbol{w}_B - \boldsymbol{K}_{P,r}\boldsymbol{e}_r - \boldsymbol{K}_{D,r}\boldsymbol{e}_w \end{aligned} \tag{27}$$

for pose control. $\boldsymbol{K}_{P,f}$, $\boldsymbol{K}_{I,f}$, $\boldsymbol{K}_{P,m}$, $\boldsymbol{K}_{I,m}$, $\boldsymbol{K}_{P,t}$, $\boldsymbol{K}_{D,t}$, $\boldsymbol{K}_{P,r}$, and $\boldsymbol{K}_{D,r}$ are diagonal positive definite gain matrices. $\boldsymbol{e}_f = \boldsymbol{f}_c - \boldsymbol{f}_d$, $\boldsymbol{e}_m = \boldsymbol{\tau}_c - \boldsymbol{\tau}_d$, $\boldsymbol{e}_t = \boldsymbol{p}_B - \boldsymbol{p}_{B,d}$, and $\dot{\boldsymbol{e}}_t = \boldsymbol{v}_B - \boldsymbol{v}_{B,d}$ represent the force, moment, position, and velocity error, respectively. The orientation error and the body angular velocity error are expressed as:

$$\begin{aligned} \boldsymbol{e}_r &= \frac{1}{2}(\boldsymbol{R}_{B,d}^T\boldsymbol{R}_B - \boldsymbol{R}_B\boldsymbol{R}_{B,d}^T)^\vee, \\ \boldsymbol{e}_w &= \boldsymbol{w}_B - \boldsymbol{R}_B^T\boldsymbol{R}_{B,d}(\boldsymbol{R}_{B,d}^T\dot{\boldsymbol{R}}_{B,d})^\vee, \end{aligned} \tag{28}$$

where the vee operator $(\cdot)^\vee : \mathfrak{so}(3) \mapsto \mathbb{R}^3$ is the inverse of the hat operator. $\boldsymbol{f}_c$ and $\boldsymbol{\tau}_c$ represent the contact force and torque measured by F/T sensor, while $\boldsymbol{f}_d$ and $\boldsymbol{\tau}_d$ denote the desired contact force and torque, respectively. To compensate for the external wrench at the end-effector during contact, we added an extra input term to the wrench command. Therefore, the final wrench command is:

$$\mathbf{w}_{\mathrm{fin}} = \mathbf{w} + \begin{bmatrix} \mathbf{0}_3 \\ \boldsymbol{r}_{\mathrm{com}} \times \boldsymbol{f}_c + \boldsymbol{\tau}_c \end{bmatrix}, \tag{29}$$

where $\boldsymbol{r}_{\mathrm{com}}$ represents the offset from the system's center of mass to the end-effector.

The optimized drone system (recall Table I) is simulated in PyBullet [26] environments with 1kHz control frequency. The simulation scenario is set as follows.

- $t = 0\mathrm{s} - 5\mathrm{s}$: hovering
- $t = 5\mathrm{s} - 15\mathrm{s}$: applying contact wrench to an object
- $t = 15\mathrm{s} - 25\mathrm{s}$: maintaining contact

During maintaining contact ($t = 15\mathrm{s} - 25\mathrm{s}$), the final contact wrench on the object is set as $[45,\ 0,\ mg,\ 0,\ 0,\ 0]^T$ and $\boldsymbol{R}_{B,d} = \boldsymbol{I}_3$. To this end, the contact wrench profile is determined by quintic polynomial trajectories, while the orientation is controlled to maintain $\boldsymbol{R}_{B,d} = \boldsymbol{I}_3$.

The simulation results are shown in Fig. 8. During hovering ($t = 0\mathrm{s} - 5\mathrm{s}$), the proposed drone can generate the optimized rotor input $\boldsymbol{u}_h$, as shown in Fig. 8(c). While applying the contact wrench to the object ($t = 5\mathrm{s} - 15\mathrm{s}$) and maintaining contact ($t = 15\mathrm{s} - 25\mathrm{s}$), the drone's body force tracks the force trajectories $\boldsymbol{f}_d$ and converges to the final contact wrench $[45,\ 0,\ mg,\ 0,\ 0,\ 0]^T$ with small errors, as shown in Fig. 8(a) and 8(b). Throughout this scenario, all rotor inputs exhibit feasible forces within the bounds, as shown in Fig. 8(c). As a consequence, this simulation verifies that the designed drone can generate the RW while satisfying the given rotor input saturation.

V. CONCLUSION

In this paper, we present a design framework for a fully actuated drone with non-isotropic wrench shape for aerial contact manipulation. To achieve this, we explicitly define the RW, taking into consideration contact manipulation. By utilizing the hyperplane shifting method, we reformulate RW as an appropriate constraint function that can be integrated into the optimization problem. Consequently, the resulting fully actuated drone design satisfies wrench feasibility for a user-defined RW. The hovering thrust force is used as the cost function to minimize the hovering energy consumption. As a result, our proposed drone exhibits a significant improvement over the typical fully actuated system, with a hovering force efficiency of 0.7610, more than doubled, and a contact force efficiency of 0.8245, nearly 1.4 times higher. To verify our approach, a simulation with hybrid wrench and pose control is also conducted.

In future work, we will consider multiple RW cases with different orientations to handle a range of contact manipulation scenarios. Moreover, we plan to integrate the rotor locations and spinning axes of the propellers into the optimization problem. This will enable us to account for aerodynamic interactions between the propellers. Finally, we will verify the proposed method through real-world experiments.

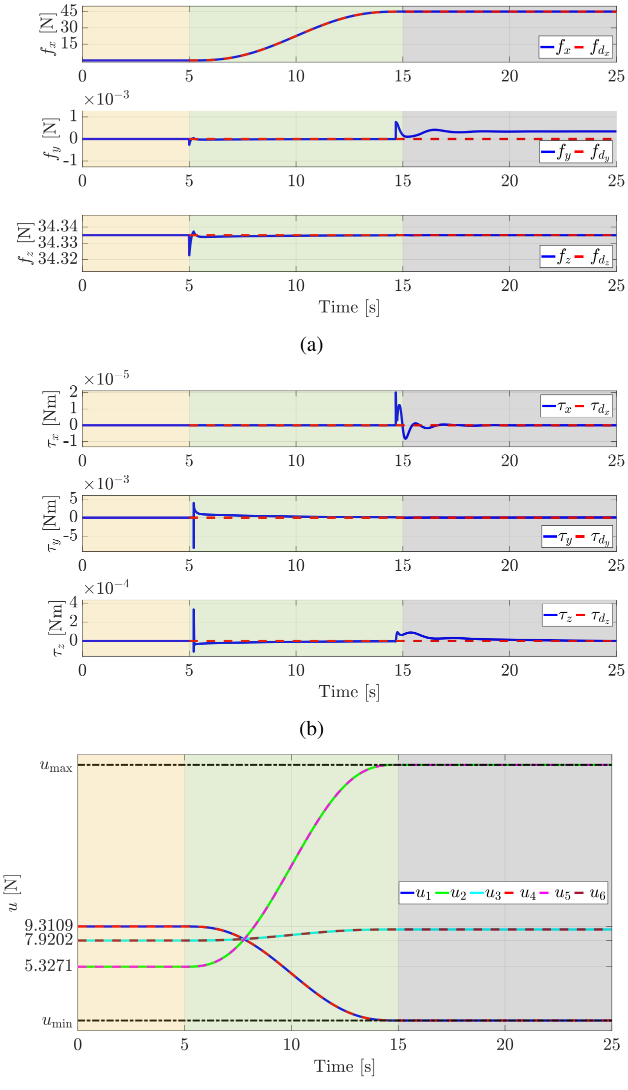

(a)

(b)

(c)

Fig. 8. Simulation results for contact wrench feasibility. The yellow, green, and dark gray correspond to hovering, generating contact force, and maintaining contact, respectively. (a) The body force during the scenarios. (b) The body torque during the scenarios. (c) The rotor input during the scenarios. The black dashed lines indicate maximum and minimum rotor input.

APPENDIX

A. Derivation of (17)

Similar to [27], the wrench $\mathbf{w} = [f_x, f_y, f_z, \tau_x, \tau_y, \tau_z]^T$ corresponding to the boundary values of (16) are written as:

$$\begin{aligned} f_x &= F_{\mathrm{h}} \sin(\theta)\cos(\phi),\ f_y = F_{\mathrm{h}} \sin(\theta)\sin(\phi), \\ f_z &= F_{\mathrm{h}} \cos(\theta),\ \tau_x = \tau_y = \tau_z = 0, \end{aligned} \tag{30}$$

where θ and ϕ are bounded from $-\pi$ to π. Since all the wrenches in (30) must satisfy all the inequalities in (8), for every $\boldsymbol{c}_j^T$ and d_j, the following j^{th} inequality must also hold:

$$\boldsymbol{c}_j^T \mathbf{w} \leq d_j. \tag{31}$$

Accordingly, the inequality (31) can be expressed as

$$\begin{aligned} F_{\mathrm{h}}(c_{j_1}\sin(\theta)\cos(\phi) + c_{j_2}\sin(\theta)\sin(\phi)) \\ + F_{\mathrm{h}}c_{j_3}\cos(\theta) \leq d_j, \end{aligned} \tag{32}$$

which is equivalent to

$$F_{\mathrm{h}}(\sin(\theta)\sqrt{c_{j_1}^2 + c_{j_2}^2} + c_{j_3}\cos(\theta)) \leq d_j, \tag{33}$$

because $c_{j_1}\cos(\phi) + c_{j_2}\sin(\phi)$ reaches its maximum when

$$\cos(\phi) = \frac{c_{j_1}}{\sqrt{c_{j_1}^2 + c_{j_2}^2}},\ \sin(\phi) = \frac{c_{j_1}}{\sqrt{c_{j_1}^2 + c_{j_2}^2}}. \tag{34}$$

The inequality (33) is a function of θ, which reaches its maximum when

$$\begin{aligned} \cos(\theta) &= \frac{c_{j_3}}{\sqrt{c_{j_1}^2 + c_{j_2}^2 + c_{j_3}^2}}, \\ \sin(\theta) &= \frac{\sqrt{c_{j_1}^2 + c_{j_2}^2}}{\sqrt{c_{j_1}^2 + c_{j_2}^2 + c_{j_3}^2}}. \end{aligned} \tag{35}$$

Consequently, according to (34) and (35), the equation (30) is written as:

$$\begin{aligned} f_x &= \frac{F_{\mathrm{h}}c_{j_1}}{\sqrt{c_{j_1}^2 + c_{j_2}^2 + c_{j_3}^2}}, f_y = \frac{F_{\mathrm{h}}c_{j_2}}{\sqrt{c_{j_1}^2 + c_{j_2}^2 + c_{j_3}^2}}, \\ f_z &= \frac{F_{\mathrm{h}}c_{j_3}}{\sqrt{c_{j_1}^2 + c_{j_2}^2 + c_{j_3}^2}}, \tau_x = \tau_y = \tau_z = 0. \end{aligned} \tag{36}$$

The inequality (32) is also modified as:

$$F_{\mathrm{h}}\sqrt{c_{j_1}^2 + c_{j_2}^2 + c_{j_3}^2} \leq d_j. \tag{37}$$

REFERENCES

[1] M. J. Kim, R. Balachandran, M. De Stefano, K. Kondak, and C. Ott, "Passive Compliance Control of Aerial Manipulators," in *IEEE/RSJ International Conference on Intelligent Robots and Systems (IROS)*, 2018, pp. 4177–4184.

[2] M. J. Kim, K. Kondak, and C. Ott, "A Stabilizing Controller for Regulation of UAV With Manipulator," *IEEE Robotics and Automation Letters*, vol. 3, no. 3, pp. 1719–1726, 2018.

[3] J. Jeong and M. J. Kim, "Passivity-based Decentralized Control for Collaborative Grasping of Under-Actuated Aerial Manipulators," in *IEEE International Conference on Robotics and Automation (ICRA)*, 2023, pp. 7699–7705.

[4] R. Rashad, J. Goerres, R. Aarts, J. B. C. Engelen, and S. Stramigioli, "Fully Actuated Multirotor UAVs: A Literature Review," *IEEE Robotics & Automation Magazine*, vol. 27, no. 3, pp. 97–107, 2020.

[5] M. Hamandi, F. Usai, Q. Sablé, N. Staub, M. Tognon, and A. Franchi, "Design of multirotor aerial vehicles: A taxonomy based on input allocation," *The International Journal of Robotics Research*, vol. 40, no. 8-9, pp. 1015–1044, 2021.

[6] S. Rajappa, M. Ryll, H. H. Bülthoff, and A. Franchi, "Modeling, control and design optimization for a fully-actuated hexarotor aerial vehicle with tilted propellers," in *IEEE International Conference on Robotics and Automation (ICRA)*, 2015, pp. 4006–4013.

[7] R. Rashad, P. Kuipers, J. Engelen, and S. Stramigioli, "Design, modeling, and geometric control on SE (3) of a fully-actuated hexarotor for aerial interaction," *arXiv preprint arXiv:1709.05398*, 2017.

[8] Y. S. Sarkisov, M. J. Kim, D. Bicego, D. Tsetserukou, C. Ott, A. Franchi, and K. Kondak, "Development of SAM: cable-Suspended Aerial Manipulator," in *International Conference on Robotics and Automation (ICRA)*, 2019, pp. 5323–5329.

[9] G. Jiang, R. Voyles, K. Sebesta, and H. Greiner, "Estimation and optimization of fully-actuated multirotor platform with nonparallel actuation mechanism," in *IEEE/RSJ International Conference on Intelligent Robots and Systems (IROS)*, 2017, pp. 6843–6848.

[10] M. Tognon and A. Franchi, "Omnidirectional Aerial Vehicles With Unidirectional Thrusters: Theory, Optimal Design, and Control," *IEEE Robotics and Automation Letters*, vol. 3, no. 3, pp. 2277–2282, 2018.

[11] A. Nikou, G. C. Gavridis, and K. J. Kyriakopoulos, "Mechanical design, modelling and control of a novel aerial manipulator," in *IEEE International Conference on Robotics and Automation (ICRA)*, 2015, pp. 4698–4703.

[12] D. Brescianini and R. D'Andrea, "Design, modeling and control of an omni-directional aerial vehicle," in *IEEE International Conference on Robotics and Automation (ICRA)*, 2016, pp. 3261–3266.

[13] S. Park, J. Lee, J. Ahn, M. Kim, J. Her, G.-H. Yang, and D. Lee, "ODAR: Aerial Manipulation Platform Enabling Omnidirectional Wrench Generation," *IEEE/ASME Transactions on Mechatronics*, vol. 23, no. 4, pp. 1907–1918, 2018.

[14] M. Ryll, D. Bicego, and A. Franchi, "Modeling and control of FAST-Hex: A fully-actuated by synchronized-tilting hexarotor," in *IEEE/RSJ International Conference on Intelligent Robots and Systems (IROS)*, 2016, pp. 1689–1694.

[15] M. Ryll, D. Bicego, M. Giurato, M. Lovera, and A. Franchi, "FAST-Hex—A Morphing Hexarotor: Design, Mechanical Implementation, Control and Experimental Validation," *IEEE/ASME Transactions on Mechatronics*, vol. 27, no. 3, pp. 1244–1255, 2022.

[16] Y. Aboudorra, C. Gabellieri, R. Brantjes, Q. Sablé, and A. Franchi, "Modelling, Analysis, and Control of OmniMorph: an Omnidirectional Morphing Multi-rotor UAV," *Journal of Intelligent & Robotic Systems*, vol. 110, no. 1, p. 21, 2024.

[17] M. Ryll, H. H. Bülthoff, and P. R. Giordano, "A Novel Overactuated Quadrotor Unmanned Aerial Vehicle: Modeling, Control, and Experimental Validation," *IEEE Transactions on Control Systems Technology*, vol. 23, no. 2, pp. 540–556, 2015.

[18] T. Anzai, M. Zhao, M. Murooka, F. Shi, K. Okada, and M. Inaba, "Design, Modeling and Control of Fully Actuated 2D Transformable Aerial Robot with 1 DoF Thrust Vectorable Link Module," in *IEEE/RSJ International Conference on Intelligent Robots and Systems (IROS)*, 2019, pp. 2820–2826.

[19] M. Allenspach, K. Bodie, M. Brunner, L. Rinsoz, Z. Taylor, M. Kamel, R. Siegwart, and J. Nieto, "Design and optimal control of a tiltrotor micro-aerial vehicle for efficient omnidirectional flight," *The International Journal of Robotics Research*, vol. 39, no. 10-11, pp. 1305–1325, 2020.

[20] H. Hussein, J. C. Santos, and M. Gouttefarde, "Geometric Optimization of a Large Scale CDPR Operating on a Building Facade," in *IEEE/RSJ International Conference on Intelligent Robots and Systems (IROS)*, 2018, pp. 5117–5124.

[21] S. Bouchard, C. Gosselin, and B. Moore, "On the ability of a cable-driven robot to generate a prescribed set of wrenches," *Journal of Mechanisms and Robotics*, vol. 2, no. 1, 2010.

[22] P. Bosscher, A. Riechel, and I. Ebert-Uphoff, "Wrench-feasible workspace generation for cable-driven robots," *IEEE Transactions on Robotics*, vol. 22, no. 5, pp. 890–902, 2006.

[23] M. Gouttefarde and S. Krut, "Characterization of parallel manipulator available wrench set facets," in *Advances in Robot Kinematics: Motion in Man and Machine: Motion in Man and Machine*. Springer, 2010, pp. 475–482.

[24] G. Michieletto, M. Ryll, and A. Franchi, "Fundamental Actuation Properties of Multirotors: Force–Moment Decoupling and Fail–Safe Robustness," *IEEE Transactions on Robotics*, vol. 34, no. 3, pp. 702–715, 2018.

[25] E. Dyer, S. Sirouspour, and M. Jafarinasab, "Energy Optimal Control Allocation in a Redundantly Actuated Omnidirectional UAV," in *International Conference on Robotics and Automation (ICRA)*, 2019, pp. 5316–5322.

[26] E. Coumans and Y. Bai, "Pybullet, a python module for physics simulation for games, robotics and machine learning," 2016.

[27] M. Gouttefarde, J.-F. Collard, N. Riehl, and C. Baradat, "Geometry Selection of a Redundantly Actuated Cable-Suspended Parallel Robot," *IEEE Transactions on Robotics*, vol. 31, no. 2, pp. 501–510, 2015.